Shock Waves (2013) 23:39–53
DOI 10.1007/s00193-012-0400-0

ORIGINAL ARTICLE

Blast wave mitigation by dry aqueous foams

E. Del Prete · A. Chinnayya · L. Domergue · A. Hadjadj · J.-F. Haas

Received: 21 February 2012 / Revised: 14 May 2012 / Accepted: 13 June 2012 / Published online: 2 August 2012

Abstract This paper presents results of experiments and numerical modeling on the mitigation of blast waves using dry aqueous foams. The multiphase formalism is used to model the dry aqueous foam as a dense non-equilibrium two-phase medium as well as its interaction with the high explosion detonation products. New experiments have been performed to study the mass scaling effects. The experimental as well as the numerical results, which are in good agreement, show that more than an order of magnitude reduction in the peak overpressure ratio can be achieved. The positive impulse reduction is less marked than the overpressures. The Hopkinson scaling is also found to hold particularly at larger scales for these two blast parameters. Furthermore, momentum and heat transfers, which have the main dominant role in the mitigation process, are shown to modify significantly the classical blast wave profile and thereafter to disperse the energy from the peak overpressure due to the induced relaxation zone. In addition, the velocity of the fireball, which acts as a piston on its environment, is smaller than in air. Moreover, the greater inertia of the liquid phase tends to project the aqueous foam far from the fireball. The created gap tempers the amplitude of the transmitted shock wave to the aqueous foam. As a consequence, this results in a lowering of blast wave parameters of the two-phase spherical decaying shock wave.

Keywords Blast wave · Mitigation · Aqueous foams · Multiphase Modeling

Communicated by O. Igra.

E. Del Prete · A. Chinnayya (✉) · A. Hadjadj
CORIA CNRS UMR 6614, Site Universitaire du Madrillet, 76800 Saint-Etienne du Rouvray, France
e-mail: chinnayya@coria.fr; ashwin.chinnayya@coria.fr

E. Del Prete · L. Domergue · J.-F. Haas
CEA, DAM, DIF, 91297 Arpajon Cedex, France

Present Address:
L. Domergue
CEA, DAM, Le Ripault, 37260 Monts, France

1 Introduction

Blast waves from very intense explosion can cause widespread human, material or environmental damages. Its mitigation is therefore of great concern. The use of aqueous foam (AF) barrier belongs to modern protective technology, such as fire suppression, shock and blast waves mitigation. Due to their relative easy availability, they have presented an attractive option since the 80's [38] for military as well as civilian blast mitigation technologies and design methodologies.

The sudden release of energy in air coming from any process can cause the propagation of blast wave (BW). It is a sharp jump of pressure followed by a pressure decrease [17,18]. Blast effects from unconfined charges have been studied for many years. Pioneering work on point explosion is reported by Taylor [46]. When the detonation wave propagating through a condensed explosive reaches the air interface, an intense shock wave (up to several hundred bars) propagates radially outwards through the air. The strength of this BW can be shown to be greatly attenuated when it propagates in a two-phase aqueous media [17,18]. One example can be quoted from the book of Needham [31] where a detonation shot of the Koon nuclear device took place during a rainstorm. A 20 % peak overpressure reduction was measured as compared with the overpressures registered in the non-rainy part. Several aqueous two-phase media can be mentioned as attenuating media, in increasing order of mass loading: mist [43], foam, snow [23]. Density of mist is around 1 kg/m^3,

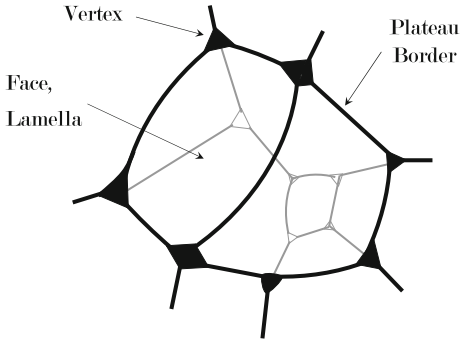

Fig. 1 Structure of an aqueous dry foam. Liquid films meet at plateau borders (*PB*), which merge at vertices

whereas it is closer to 10 kg/m^3 for foams. In the past 30 years, several research groups have investigated [6,15,20] the efficiency of aqueous foam to mitigate blast and sound waves [38,39]. First experimental results from Winfield et al. [48] reported overpressure reduction of five to ten for reduced distances over one. The wave speed was divided by two.

An aqueous foam is a cellular two-phase system in which gas cells are enclosed by thin liquid films [47]. The gaseous phase is dispersed in bubbles, whereas the liquid is the continuous phase. The bubbles take the form of polyhedral cells (see Fig. 1), with liquid surfaces meeting in lines and lines merging at vertices. The lines are Plateau Borders (PB)—after J.A. Plateau [36] who was the first to describe the foam structure in the late nineteenth century. PB are channels of finite width where the liquid is mainly to be found. This topological description corresponds to a *dry foam*. As liquid volume fraction increases, PB swell and bubbles progressively recover their spherical shapes and the foam evolves into a *wet foam*. Any further increase of liquid will allow the bubbles to come apart and the foam becomes a *bubbly liquid*. To summarize the resulting spectrum of the aqueous foam medium, the following classification according to the value of the liquid volume fraction α_1 can be made [9,40]: as for dry foams, $\alpha_1 \leq 0.05$, whereas $0.05 < \alpha_1 \leq 0.36$ for wet foams, and $0.36 < \alpha_1$ for bubbly liquids. The liquid is a mixture of water and little surfactant. This article deals only with water-based foams. Britan et al. [7,9] have dealt with the inclusion of solid particles, which will lodge themselves into the vertices and the PB of the cellular structure of the foam. Their role is to shield and armor the frame of the aqueous foam cellular structure. Indeed, water-based foam is metastable and even instable and its lifetime due to coarsening and drainage is necessarily limited. Under operational conditions, the expansion ratio (ER) expression is somewhat preferred. It is defined as the ratio of the foam volume to the water volume. Then $ER \simeq 1/\alpha_1$ when the foam density is much greater than the gas density. In the case of dry foams, the liquid volume fraction can be linked to the ratio of the radius of curvature r of the PB and to the cross-section of the bubble D [47] $\alpha_1 = \tilde{c}r^2/(D/2)^2$; $\tilde{c}$ is a geometrical quantity which depends on the structure of the foam. For a Kelvin structure, $\tilde{c} \simeq 1/3$ [47].

Various mechanisms can be responsible for the mitigation: the momentum transfer, the heat transfer and the liquid evaporation. These transfers occur between the detonation products, the gas and the liquid phases. Since aqueous foams are natural but in metastable states, the liquid lattice is likely to be shattered into more stable droplets under high-pressure ratio shock-wave impingement [8]. Indeed, after the shock passage, the films exhibit strong acceleration and are then rapidly blown away. The stability of the aqueous foam is due to the presence of these films. Therefore the lattice of the foam, which is composed of Plateau Borders, becomes dislocated and this liquid web fractures. After this collapse, the surface tension tends to form spherical droplets from the liquid ligaments. This has led Britan and co-workers [8,10] to model the process of shock-wave attenuation in shock tubes by a foam screen using a gaseous suspension of water droplets, whose characteristic size is the radius of the PB. Hence, the specific surface increases and enhances the interphase transfer. Crepeau et al. [13] showed that the main contributions to mitigation were momentum extraction and heat transfer due to the presence of higher heat capacity materials. When comparing their numerical results with that of the Sandia tests [20], they found that the phase change overestimates the attenuation at large reduced radii. Allen et al. [1] made comparisons between experiments and numerical modeling with the two-phase Baer and Nunziato model [2,3]. They found that the inertial effects were preponderant and that the evaporation played a secondary role for free-field blast mitigation. Similar conclusions were drawn by Schwer and Kailasanath [43] in a numerical study on the mitigation of BW by water-mist, and this was due to the low temperature downstream of the shock. These results stand for middle field range. Far from the charge, the foam will sustain the compression wave strength, which has become weaker. Over mitigation mechanisms that involve the microstructure will then take over, such as film pulsation, interstitial PB flow and heat conduction [19].

The aim of this article was to conduct new experiments corroborated by a numerical study and to shed more light on the physical mechanisms underlying the BW mitigation by dry aqueous foams and to ascertain to which extent the scaling laws are reliable. The numerical results from a multiphase model will be compared with the experimental data. The paper is organized as follows: Sect. 2 describes the multiphase model as well as the different constitutive relations related to this model. Section 3 recalls the different speeds of sound at which the pressure waves propagate in a multiphase flow. Section 4 describes the two experimental setups for full and sub-scale experiments. In Sect. 5, the numerical results

are compared with the collected experimental data from literature and to the present measurements. Conclusions are drawn in Sect. 6.

2 Mathematical and numerical modeling

2.1 Two-phase hydrodynamic model

The multifluid model [12] used in this study is a model which does not assume any thermo-mechanical equilibrium. Indeed, the passage of shock wave over a two-phase system will bring the two phases to different mechanical and thermodynamic states, due to the impedance contrast. Relaxation processes will attempt to erase these differences and edge the phases towards equilibrium. From a mathematical viewpoint, this model is unconditionally hyperbolic. It is written in spherical coordinates, r being the radial coordinate. The system of equations for the k^{th} phase is the following:

$$\begin{aligned}
&\frac{\partial \alpha_k}{\partial t} + u_i \frac{\partial \alpha_k}{\partial r} = \mu_k \Delta P - \frac{\dot{m}_k}{\rho_\Gamma} \\
&\frac{\partial (\alpha\rho)_k}{\partial t} + \frac{\partial (\alpha\rho u)_k}{\partial r} = -\frac{2(\alpha\rho u)_k}{r} - \dot{m}_k \\
&\frac{\partial (\alpha\rho u)_k}{\partial t} + \frac{\partial (\alpha\rho u^2 + \alpha P)_k}{\partial r} = P_i \frac{\partial \alpha_k}{\partial r} - \frac{2(\alpha\rho u^2)_k}{r} \\
&\quad + F_{dk} - \dot{m}_k u_\Gamma \\
&\frac{\partial (\alpha\rho E)_k}{\partial t} + \frac{\partial (\alpha\rho E u + \alpha P u)_k}{\partial r} = P_i u_i \frac{\partial \alpha_k}{\partial r} - \frac{2(\alpha\rho u H)_k}{r} \\
&\quad + F_{dk} u_I - P_I^{'} \mu_k \Delta P + Q_{Ik} + \dot{m}_k \left(H_{\Gamma k} - \frac{P_I^{'}}{\rho_\Gamma} \right)
\end{aligned} \tag{1}$$

where α_k, ρ_k, u_k, P_k are, respectively, the volume fraction, the density, the material velocity and the pressure of each phase. The saturation constraint is $\alpha_1 + \alpha_2 = 1$, where the underscript 1 denotes the liquid phase and 2 the gas phase. The total energy E_k for each phase is the sum of the internal energy and the kinetic energy, $E_k = e_k + \dfrac{u_k^2}{2}$ and the total enthalpy is given by $H_k = E_k + \dfrac{P_k}{\rho_k}$.

The pressure relaxation process is represented by $\mu_k \Delta P$. Whatever the two-phase topology, the pressure relaxation coefficient is given by $\mu_1 = -\mu_2 = A_I/2(Z_1 + Z_2)$, A_I, the interface surface per unit volume. It has been shown that in practical situations, the pressure relaxation time scale is associated with the dissipation of acoustic waves into the multiphase control volume [12,35] and is several orders of magnitude lower than the other relaxation time scales.

The momentum interphase interaction is represented by the drag force F_{dk}, which express the velocity relaxation and the drag between phases. The variables with underscript Γ are interfacial variables relative to the mass transfer $\dot{m}$. Q_{Ik} represents the heat transfer associated with the phase k. The acoustic impedance for each phase k is $Z_k = \rho_k c_k$, where c_k is the speed of sound of the phase k.

$$\begin{aligned}
&u_I = \frac{Z_1 u_1 + Z_2 u_2}{Z_1 + Z_2}, \quad P_I = \frac{Z_2 P_1 + Z_1 P_2}{Z_1 + Z_2} \\
&u_i = u_I + \text{sign}\left(\frac{\partial \alpha_1}{\partial x}\right) \frac{P_1 - P_2}{Z_1 + Z_2}, \\
&P_i = P_I + \text{sign}\left(\frac{\partial \alpha_1}{\partial x}\right) \frac{Z_1 Z_2}{Z_1 + Z_2} (u_1 - u_2)
\end{aligned} \tag{2}$$

The interfacial variables with underscript "i" and "I" have been developed in Chinnayya et al. [12]. u_i and P_i are, respectively, the average interfacial velocity and pressure that exert at the boundaries of the two-phase control volume. These two quantities apply on volume-fraction gradients. They play a key role on material interfaces which separate non-miscible fluids. They enable continuity of velocity and pressure across an interface in the model. The mean velocity and pressure inside a two-phase control volume are u_I and P_I. The mechanical equilibrium is achieved as the outcome of the pressure and velocity relaxation processes. The thermodynamic equilibrium is achieved as the outcome of the temperature relaxation process, that is the heat transfer and phase transition steps.

The model is completed with the following topological equation for the number of liquid entities:

$$\frac{\partial n}{\partial t} + \frac{\partial (n u_1)}{\partial x} = \dot{n} \tag{3}$$

from which we can deduce the diameter of the liquid entity

$$d = \left(\frac{6\alpha_1}{\pi n} \right)^{1/3} \tag{4}$$

2.2 Heat and mass transfer

The heat fluxes $Q_{I,k}$ are usually described by the following expressions:

$$Q_{I,k} = h_k (T_I - T_k) \tag{5}$$

h_1 is the convective heat coefficient relative to the liquid phase. The heart of the liquid phase and the gas/liquid interface are thermally out of equilibrium. This expression enables to take into account the heating of the liquid phase. h_2 is the gaseous convective heat coefficient and T_I is the mean of the interfacial temperatures. The amount of heat received by the liquid is the one given by the gaseous phase.

$$h_1 (T_I - T_1) + h_2 (T_I - T_2) = 0$$

which provides the interface temperature

$$T_I = \frac{h_1 T_1 + h_2 T_2}{h_1 + h_2} \tag{6}$$

This leads to an expression for the heat transfer:

$$Q_{I,k} = h_k \left(\frac{h_1 T_1 + h_2 T_2}{h_1 + h_2} - T_k \right) \tag{7}$$

Here a spherical droplet of diameter d is considered. From the model, we can get the mean internal energy and thereby the mean temperature. The Laplacian of the temperature inside the droplet is supposed to be null. With the surface temperature T_I and the mean temperature T_k, it is possible to solve the latter equation and to show that the liquid Nusselt number, which is the ratio between the total heat transfer and the conduction heat transfer is equal to 4. The thermal conductivity of liquid water is $\lambda_1 \approx 0.6$ W/mK.

The convective heat coefficient can be obtained from experimental correlations [25], as a function of the Nusselt number

$$h_k = \frac{\lambda_k}{d} n N u_k S_d \tag{8}$$

The Nusselt number for the gas is

$$N u_2 = 2 + 0.6 R e_d^{1/2} P r^{1/3} \tag{9}$$

The droplet Reynolds number is defined by

$$R e_d = \frac{\rho_2 \left| u_1 - u_2 \right| d}{\mu_2} \tag{10}$$

with μ_2 the dynamic viscosity of the gaseous phase as function of the gas temperature $\mu_2 = \mu_2^0 \left(\frac{T}{T_0} \right)^{0.76}$, with $\mu_2^0 = 1.71.10^{-5}$ kg/m s and $T_0 = 273$ K. The thermal conductivity of the air is determined from the Prandtl number, which is the ratio between the viscosity and the thermal diffusivity $Pr = \frac{\mu_2 C_{p2}}{\lambda_2} = 0.7$. The calorific heat coefficient C_{p2} is equal to 1 kJ/kg K.

2.3 Drag force

Three different forces act on the droplets : the shear forces, the inertial forces which tend to deform the droplet and the surface tension forces acting to retain its initial form. The Weber number $We = \frac{\rho_2 \left| u_2 - u_1 \right|^2 d}{\sigma}$ is the ratio between the inertial forces and the surface tension forces; σ is the surface tension gas/liquid. $Oh = \frac{\mu_1}{\sqrt{\rho_1 d \sigma}}$ is the Ohnesorge number, which is the ratio between the shear forces within the droplet and the surface tension forces. The first response of the drop, after it is exposed to a high-speed airstream, is a flattening of the drop. The drop also accelerates but does not move significantly. The second step is a constant acceleration of the droplet. Thus the drag coefficient which includes these two steps can be cast into the form [33],

$$C_\mathrm{d} = 1.6 + 0.4 O h^{0.08} W e^{0.01} \tag{11}$$

and the drag force becomes

$$F_\mathrm{d} = \frac{3\alpha_1}{4d} C_\mathrm{d} \rho_2 (u_2 - u_1) \left| u_2 - u_1 \right| \tag{12}$$

2.4 Numerical resolution

The proposed model can be cast in the following form:

$$\frac{\partial}{\partial t} (\alpha W)_k + \frac{\partial}{\partial r} (\alpha F)_k = F_k^{\mathrm{lag}} \times \frac{\partial \alpha_k}{\partial r} + S_{\mathrm{geom},k} + S_{\mathrm{d},k} \tag{13}$$

where α_k, $W = (1,\ \rho,\ \rho u,\ \rho E)$, $F = \left(0,\ \rho u,\ \rho u^2 + P,\ \rho E u + P u\right)$, $F^{\mathrm{lag}} = (u_i,\ 0,\ P_i,\ P_i u_i)$ are, respectively, the volume fraction, the fluid conservative variable, the fluid eulerian flux and the Lagrangian fluid flux, respectively. The interfacial variables are obtained from the homogenization Discrete Equation Method (DEM) [12]. $S_{\mathrm{geom},k}$ stands for the spherical divergence and $S_{d,k}$ accounts for the momentum and the energy exchanges between phases. The overall strategy of resolution is based on the Strang splitting scheme, detailed in [12]. The pressure relaxation is infinite and follows the numerical resolution proposed in [26].

3 Speed of sound in two-phase mixtures

The first statement comes from the hyperbolic analysis of the two-fluid model without source terms. The complete set of homogeneous equations without source terms can be written in the primitive form:

$$\frac{\partial W}{\partial t} + A(W) \frac{\partial W}{\partial x} = 0$$

The propagation waves are obtained from the eigenvalues of the Jacobian matrix $A(W)$: for the liquid phase, $\lambda = u_1 - c_1, u_1, u_1 + c_1$, for the gaseous phase, $\lambda = u_2 - c_2, u_2, u_2 + c_2$ with the interface velocity $\lambda = u_i$.

The second statement is that the speed of sound of the two-phase mixtures can reach low values, even in the limit of low liquid volume fractions. In general, the two-phase speed of sound is below the speed of sound of the pure fluids, due to the contrast of acoustic properties. The mixture density is dominated by the liquid density and its compressibility by the gas phase. Consequently, as the liquid volume fraction is increased, the effective two-phase media becomes impenetrable to pressure waves propagation. The speed of sound of the two-phase mixture, in mechanical equilibrium, can be identified with the sound speed of Wood c_W:

$$\frac{1}{\rho_m c_W^2} = \frac{\alpha_1}{\rho_1 c_1^2} + \frac{\alpha_2}{\rho_2 c_2^2} \tag{14}$$

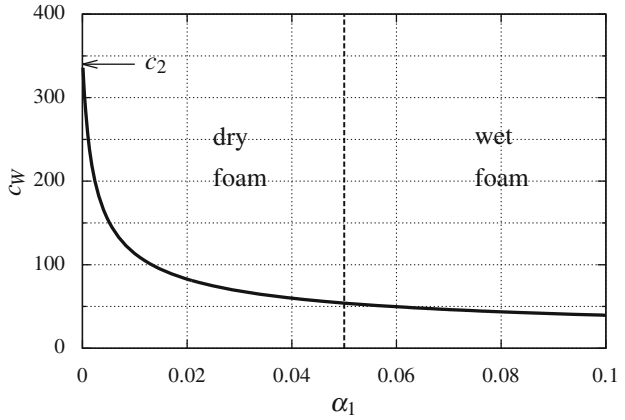

Fig. 2 Speed of sound of Wood (m/s) in a mixture of gas–water as a function of the liquid volume fraction α_1 between 0. and 0.1. The *arrow* denotes the speed of sound of the gas $c_2 = 340$ m/s

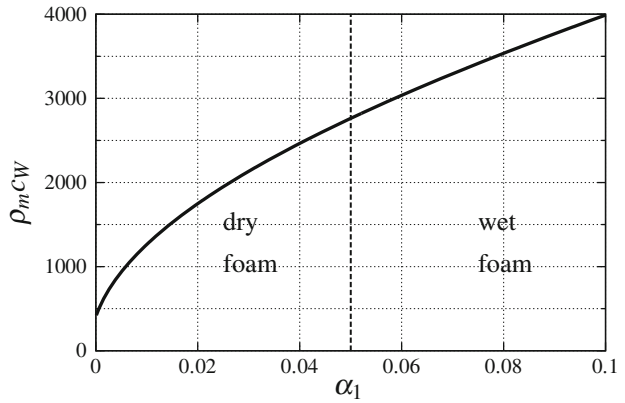

Fig. 3 Acoustic impedance (kg/m^2 s) in a mixture of gas–water as a function of the liquid volume fraction α_1 between 0. and 0.1

where $\rho_m = \alpha_1\rho_1 + \alpha_2\rho_2$ is the mixture density of the two-phase mixture. In the present model, when the pressure and velocity relaxation coefficients tend to infinity, an asymptotic model can be obtained [12]. A hyperbolic analysis of the reduced model exhibits the speed of sound of Wood as the speed of propagation of the two-phase pressure waves. This speed has been used as an indirect method by [16] to determine experimentally the liquid volume fraction in aqueous foams.

Figures 2 and 3 show, respectively, the evolution of the sound speed of Wood c_W and the acoustic impedance $\rho_m c_W$ of a two-phase mixture composed of air and water for a volume fraction varying between 0 and 0.1. As it can be seen, this speed of sound exhibits a non-monotonous variation over the whole range of the volume fraction. When the liquid volume fraction is below 0.1, the speed of sound decreases, whereas the acoustic impedance increases.

4 Experimental setup

This section describes two different experimental configurations. The first one deals with a full-scale installation, involving several kg of high explosive (HE) of Plastrite PLANP, which is a French military explosive, close to Semtex® or C4. The second set of experiments concerns a sub-scale test using hundreds of grams of HE. From the overpressure signals, we determined the peak overpressure, the time of arrival of the incident shock as well as the positive impulses. For each case, a preliminary shot is performed in air and the obtained results are compared with the Kinney and Graham database [24] for validation. Further validations are made on the scaling law. As shown in the next section, the current data are in good agreement with the Hopkinson scaling.

4.1 Description of the experimental setup

As for the full-scale experiments, foam volume generated to confine the detonation device is close to 2,000 m^3. Figure 4 depicts the full-scale experimental configuration. The containment is a tent of a conical shape, whose diameter at the base is around 20 m and the height is around 8 m. The explosive device was suspended at a 2-m-high facility. Pressure gauges are placed at the same height, at different distances from the explosive device. Two shots were achieved: the HE masses were, respectively, 6.6 and 22.17 kg.

In the sub-scale experiments, the mass of HE is approximately 145 g. The charge is enclosed in a thin spherical plastic ball of 60 mm diameter and 14 g weight (see Fig. 5). The explosive device is suspended at a height of 1.5 m. The gauges are fixed on a gantry which is independent from the aqueous foam container. The explosive is centered by fishing wires fixed on the tank walls. The vessel volume is around 8 m^3.

The HE device and the pressure gauges are hung at a sufficient height so that the reflected waves from the ground and the tank walls in the sub-scale experiments will not alter the positive impulse measurements. Most of the measurements were taken far away from the fireball.

4.2 Explosive devices

In order to insure the sphericity of the BW, the HE is placed into a spherical envelope (having a geometrical default of ± 1 %) and ignited in its center by a detonator. For all experiments, we use PLANP, which consists of a mixture of 87 % in mass of PETN, 9.75 % of oil and 3.25 % of rubber. The rubber allows the operator to mould the explosive into a desired form in a light envelope. The diameters of the HE and the detonators can be found in Table 1. For each case, the mass

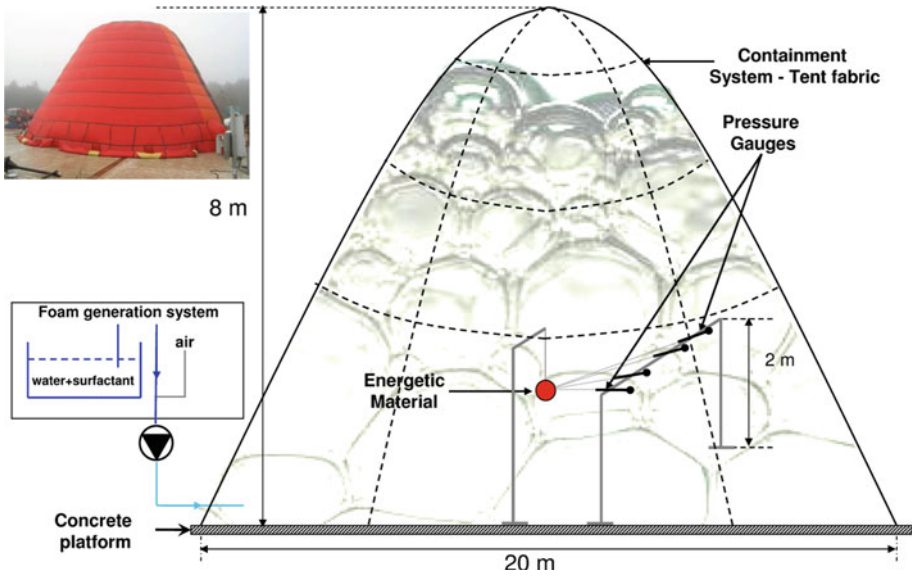

Fig. 4 Experimental configuration of full-scale experiments. Charges of 6.6 kg and 22.17 kg of PLANP at 2 m height. Pressure gauges fixed on a gantry at the same height

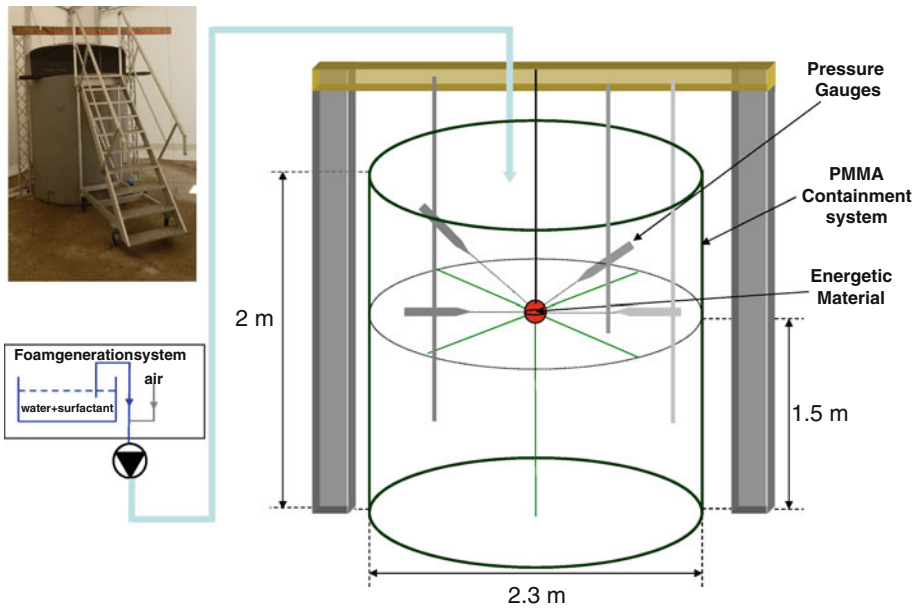

Fig. 5 Sub-scale experimental configuration. Charges of 0.145 kg of PLANP at a height of 1.5 m. Fishing wires centering the charge. Pressure gauges attached to metal rods, which are in turn attached to a gantry, independent from the tank

of HE is more than ten times greater than the mass of the envelope.

In air experiments, the envelope may have an influence on the detonation wave parameters because a part of the detonation energy is used to destroy and/or vaporize the envelope material. According to the Fano equation [31], the available energy for the blast wave can be evaluated to be at least 95 % of the initial detonation energy for the same mass loading. As the envelope is in plastic material, we assume that all the detonation wave energy is transmitted to the surrounding media, even when the latter is an aqueous foam.

The detonators used to ignite the detonation are high-voltage devices. They are made of PETN-based HE and are cylindrical. The PETN is ignited by an exploding wire. They are placed in the center of the explosive device (±2 %). For full-scale experiments, their dimensions are a little bit greater compared with sub-scale experiments (see Table 1). They are composed of 1 g and 0.2 g of PETN, respectively. The masses of detonators are small compared with the explosive device masses. We did not observe any influence of the geometry of the detonator on the sphericity of the BW. This was confirmed in the sub-scale experiments by investigation of the fireball at the

Table 1 Experimental parameters

HE mass (kg)	Media	ER	HE charge ϕ (mm)	Detonator size D × H (mm^2)	Detonator HE mass (g)	HE height (m)
6.6	Air		210	9 × 14	1	2
6.6	Foam	1:125	210	9 × 14	1	2
22.2	Foam	1:125	310	9 × 14	1	2
0.145	Air		58	6.5 × 6	0.2	2
0.145	Air		58	6.5 × 6	0.2	2
0.145	Foam	1:120	58	6.5 × 6	0.2	1.5

early stage after the detonation, with a high-speed camera Phantom.

4.3 Foam production

Prior to this study, the French Atomic Energy Commission (CEA) have developed a special aqueous foam formulation based on the use of alkyl sulfates and propylene glycol products. The foam is produced with a premix of 6 % of products in water. The premix has a viscosity of 1,800 mPa s for full-scale experiments and 4,500 mPa s for sub-scale experiment at 293 K. The surface tension is 24 mPa m. Consequently, the foam based on these formulations is particularly viscous. In comparison, the viscosity of water is 1 mPa s and its surface tension is 72 mPa m. The diameter of the bubbles is around 0.4 mm. This type of foam is experimentally studied here. All the generators used here, issued from commercial products or developed by the CEA and co-workers, are also adapted to insure a sufficient quality of the foam in terms of life time, expansion ratio and bubble homogeneity. It is worth mentioning that it is much more convenient to assure and control the foam quality in sub-scale experiments than in the full-scale one. For large-scale experiments, the generator produces foam with an expansion ratio of 1:125 at a flow rate of 40 m^3/min. This device is very heavy and does not allow producing custom foam density. For small experiments, we also created a specific scale facility which allows to produce and control accurately the foam density. The foam is produced with an expansion ratio of 1:100 at a flow rate varying from 0.150 to 1m^3/min.

4.4 Experimental supply chain

The gauges used in these experiments are PCB Piezotronics 137A20 series [37]. This series offer sensitivities of 0.014, 0.14 and 1.14 V/bar with measurement ranges from 0 to 3.45, 34.5 or 345 bar. The 137A20 series are constructed with a stable quartz piezoelectric element in Invar housing. They are piezoelectric types and are built on two levels. The charge mode pressure sensor, directly in contact with blast wave, generates a high-impedance charge output. The second level is a built-in microelectronic amplifier, which converts the high-impedance charge into a low-impedance voltage output. This type of sensor allows long wire connection without any signal loss but needs to be connected with a courant supplier. 137A20 gauges series are of pencil shape. In order to get a proper measurement of the incident wave, the pencil must be oriented perpendicularly to the shock wave and towards the charge. This type of sensor allows us to measure the side-on overpressures by limiting perturbations around the measurement element. For the experiments in foam, to protect the electrical connections, an adhesive tape was set up around plugs and cables.

Using suitable cable, sensors are connected to PCB's Series 482 signal conditioners power supply. This equipment will supply the 137A20 with a 2 to 20 mAmp constant current from +20 to +30 V DC through a current-regulating circuit. The signal can then be transmitted through long wires, unlike charge mode systems in which the system noise is a function of the cable length. ICP® sensors provide a high-voltage, low-impedance output well-suited for driving long cables through harsh environments. While there is virtually no increase in noise with ICP® sensors, the capacitive loading of the cable may distort or filter higher frequency signals depending on the supply current and the output impedance of the sensor. Generally, this signal distortion is not a problem with within a range up to 10 kHz. However, for higher frequency vibration or shock sollicitation over cables longer than 30 m, the possibility of signal distortion exists. In our experiments, the measurement chain is not longer than 20 m, so the risk of distortion is limited.

The pressure time histories are recorded on oscilloscope recorders (Lecroy Wavejet 354), which allow a maximal sampling frequency of 500 MHz. The recorder is trigged by the same signal as the detonator (delays in wires are not taken into account for this application). Then the signals are recorded on spreadsheets (Microcal Origin). With the approximation that C4 and PLANP delivered the same pressure and the same time of arrival, we used the Hartman

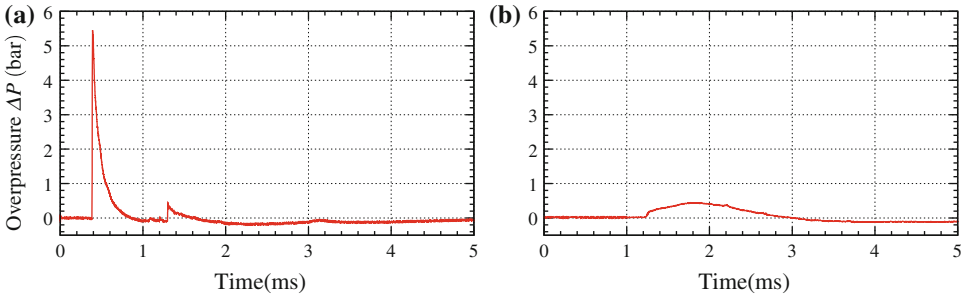

Fig. 6 Blast wave overpressure as a function of time in **a** air at a scaled distance of 1.16 m/kg$^{1/3}$ and in **b** aqueous foam at a scaled distance of 1.17 m/kg$^{1/3}$

et al. [20] fitting laws in foam to select sensor range and recorder setting. The signals are recorded on a duration of 20 ms.

5 Results and discussion

In this section, the numerical results are compared with the experimental data of BW propagation in Aqueous Foam. Table 1 recalls the experimental parameters, whereas Tables 2 and 3 (see Appendix C) summarize the experimental results obtained during the pyrotechnical campaigns. At first, to assess the mitigation properties of the aqueous foam, scaled peak overpressures and impulses of the BW are presented. Then, the time history of the different waves involved in the flow is compared with the case of air. Finally, the structure of the two-phase BW is described.

Regarding the initial conditions, we consider that the detonation is initiated at the center of the HE and that a spherical Chapman–Jouguet (CJ) detonation wave propagates into the explosive until it reaches the outer interface [30]. The detonation products are described by the Jones–Wilkins–Lee (JWL) equation of state (see Appendix A). Then an averaging procedure is done to cope with the mesh resolution of the blast calculation. For the equation of state, we can determine the detonation energy as [34] $q = \int_{v_{CJ}} P\mathrm{d}v - \frac{u_{CJ}^2}{2}$, which is needed to scale the numerical results. For all simulations, an effectiveness factor of 1.27 is taken to define the mass of TNT contained in the PLANP HE. For each calculation, the cell size of the mesh is uniform and is equal to 3 mm. The liquid volume fraction is $\alpha_1 \simeq 8.3$ ‰. The droplet size of the fragmented aqueous foam is 10 µm, which is the same order of magnitude as the PB radius. The aqueous foam is considered to be in atmospheric conditions at sea level, i.e. $P_0 = 1.01325$ bar and $T_0 = 298$ K. The properties of water have been taken.

5.1 Peak overpressures

The characteristics of BW in air and in Aqueous Foam can be compared in Fig. 6. The records of a pressure gauge at the same scaled distance have been plotted versus time, for the detonation of 145 g of PLANP. In the case of BW propagation in air, see Fig. 6a, the ideal BW pressure profile is recovered. The pressure rises abruptly to a peak overpressure, which corresponds to the primary shock. The pressure then decays to ambient during the positive phase [4], due to the expansion of the detonation products. When the case of BW propagation in AF is considered, the main difference in the structure of the BW pressure profile is that this ideal primary shock is replaced by a two-phase shock, which is indeed a partly or completely dispersed shock [41], see Fig. 6b. The decay of the compression waves then follows. The peak overpressure is therefore located at some distance of the foot of the compression waves.

The peak overpressure ratio $\Delta P/P_0$ for the experimental and numerical results are shown in Figs. 7 and 8 as a function of the scaled distance $r/W^{1/3}$, W is the TNT equivalent mass of the HE and r is the distance from the charge center. ΔP is the maximum overpressure and $P_0 = 1.01325$ bar is the initial pressure in ambient atmospheric conditions. The Kinney and Graham (KG) database is plotted as well as the Sandia fit curve [20], given by

$$\begin{aligned}\ln\left(\Delta P'\right) &= 3.7757 + 0.5085 \times \rho_{\text{foam}} \\ &\quad + (0.0695 \times \rho_{\text{foam}} - 0.0372) \\ &\quad - 3.2788 \times \ln\left(\frac{r'\rho_{\text{foam}}^{1/3}}{W'^{1/3}}\right)\end{aligned} \tag{15}$$

where $\Delta P'$ is the peak overpressure in PSI, W' is in equivalent pounds in lb of C4 and ρ_{foam} is the foam density in lb/ft^3.

Two groups of results can be distinguished. The first one refers to the results of BW in air and the second one corresponds to the BW in AF. At first, one can see the obvious good mitigation property of the aqueous foam. After a scaled distance of 0.3, the peak overpressure in AF becomes less than that in air. Indeed, at the beginning of the interaction of the detonation front with the confining medium, the total energy of the post-shock state can be estimated via linearized Riemann invariants and can be shown to decrease with the

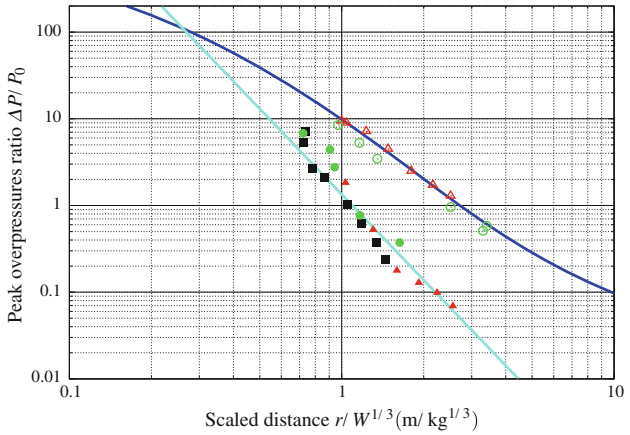

Fig. 7 Peak overpressures ratio $\Delta P/P_0$ as a function of the scaled distance $r/W^{1/3}$. Kinney and Graham database [24] (*dark blue lines*). Experimental results in air for 0.15 kg (*green circle with dot*), 6.6 kg (*red triangle with dot*). SANDIA fit [20] (*light blue lines*). Experimental results in aqueous foam, for 0.15 kg (*filled green circle*), 6.6 kg (*filled red triangle*), 22.17 kg (*black square*)

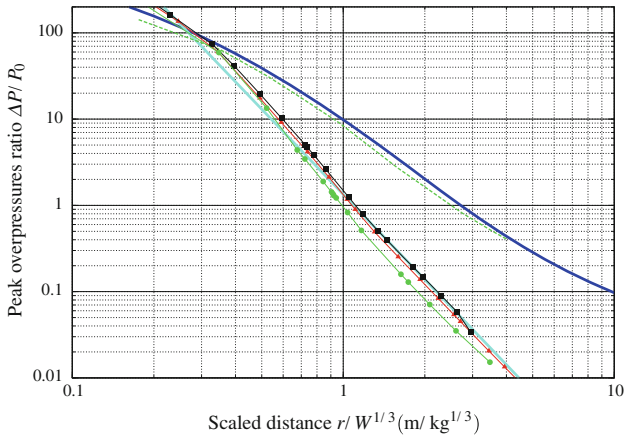

Fig. 8 Peak overpressures ratio $\Delta P/P_0$ as a function of the Scaled Distance $r/W^{1/3}$. Kinney and Graham database [24] (*dark blue lines*). Numerical results in Air for 0.15 kg (*dashed green lines*). SANDIA fit [20] (*light blue lines*). Numerical results in AF, for 0.15 kg (*green line with circle*), 6.6 kg (*red line with red triangle*), 22.17 kg (*black line with black square*)

increase of the acoustic impedance of the confining medium. This energy radiates spherically and then results in a lower overpressure. Moreover, the pressure decrease rate is much higher than that in air and the pressure reduction increases with distance. For example, in the experimental studied range of scaled distances between 1 and 3, the peak overpressure attenuation reaches 10–20. The experimental results in air (see Fig. 7) have enabled to determine the effectiveness factor of the PLANP. The experimental data in AF are slightly more scattered than that in air. They can be partly explained by the errors of distance measurements and the alignment errors of the gauges with the center of the charge. However, the experimental results follow the general trend given by the Sandia fit, showing that the Hopkinson $W^{1/3}$ scaling holds for the peak overpressures ratio.

Numerical simulations were also performed for the three charge masses (see Fig. 8). In air, there is a good agreement between the numerical results, the KG database and the measurements results. Only one curve was displayed in Fig. 8 as the results for the three masses were nearly indistinguishable. This comes from the Hopkinson $W^{1/3}$ scaling in air. In AF, the numerical results lie within the range spanned by the scattering of the experimental data. Nevertheless, there are slight differences between the results from the detonation of the three masses. This is an indication that some non-equilibrium phenomena are taking place. Less differences are apparent for the larger scale, indicating that these non-equilibrium processes have more time to reach equilibrium.

From experimental results, one can conclude that the Hopkinson $W^{1/3}$ scaling still holds, and the numerical results ascertain that this is particularly true for larger scales.

5.2 Positive pressure impulses

The positive pressure impulse is derived from the integration of the overpressure starting from the time of arrival of the blast wave t_a, along the positive time impulse t_d , corresponding to the duration for which the overpressure remains positive.

$$I^+ = \int_{t_a}^{t_a+t_d} \Delta P\,(\tau)\,\mathrm{d}\tau \tag{16}$$

The scaled positive pressure impulses $I/W^{1/3}$ for the experimental and the numerical results are shown, respectively, in Figs. 9 and 10 as a function of the scaled distance $r/W^{1/3}$. The Kinney and Graham [27] database is plotted as well as the Sandia curve fit from NEST calculator, given by

$$\ln\left(\frac{I'^+}{W'^{1/3}}\right) = 3.3379 + \frac{1}{ER}38.9908 + \ln\left(\frac{r'}{W'^{1/3}}\right)\left(-0.7681 - \frac{1}{ER}43.7811\right) \tag{17}$$

where $I'^+/W'^{1/3}$ is the scaled specific impulse in PSI ms/lb$^{1/3}$, W' is the C4-explosive equivalent mass in pounds in lb, ρ_{foam} is the foam density in lb/ft^3. ER is the expansion ratio, which is the ratio of the foam to the water volumes.

The impulses also show the mitigation property of the AF, although the impulse reduction is less than the pressure reduction. The experimental as well as the numerical results show an impulsion reduction, gradually increasing from a scaled distance above one.

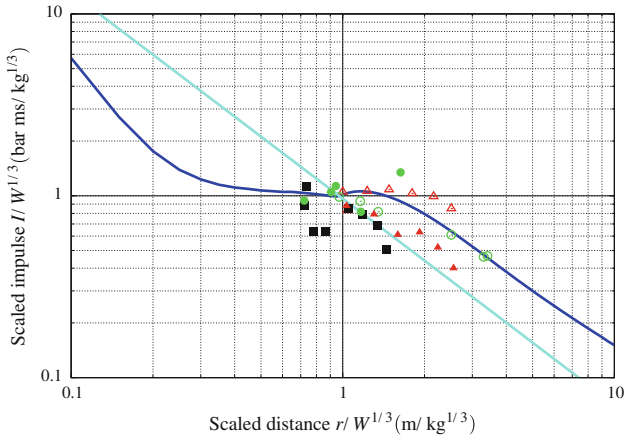

Fig. 9 Scaled positive impulse $I/W^{1/3}$ as a function of the scaled distance $r/W^{1/3}$. For legend, see caption of Fig. 7

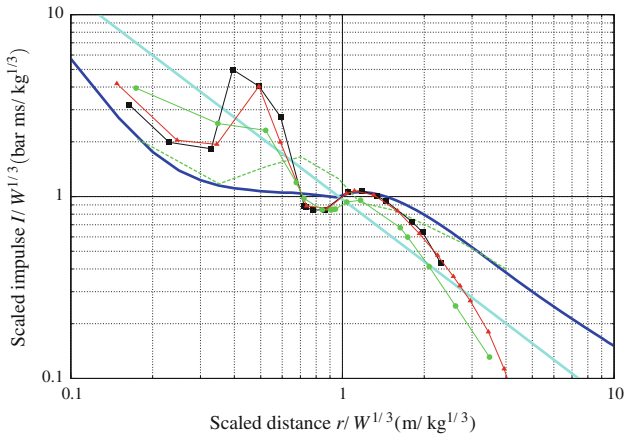

Fig. 10 Scaled positive impulse $I/W^{1/3}$ as a function of the scaled distance $r/W^{1/3}$. For legend, see caption of Fig. 8

Even if the experimental data in air and in AF are close, respectively, to the Kinney and Graham database and to the Sandia NEST fit, it can be seen that the scattering of the impulses is greater than the peak overpressures. Indeed, we have to consider the possible measurement errors linked to the use of PCB piezoelectronic gauges. Despite their good behavior under shock loading, they have to be used carefully for impulse measurements. Particular attention of gauges discharge time under solicitation has to be paid. The Discharge Time Constant (DTC) of PCB 137A20 gauges series is around 200 ms. The measured value of a constant level of static pressure decreases exponentially by a factor of 1 % every 0.01 × DTC. The positive impulse duration is at its maximum at about 10 ms for the gauges placed in foam and far from the HE charge. This gives measurement errors of 10 % at this time. In air experiments, the proximity of the fireball could also disturb this measurement although the gauges placed close to the HE are protected from heat by a thin layer of silicon. In air, the discrepancy between experiments and

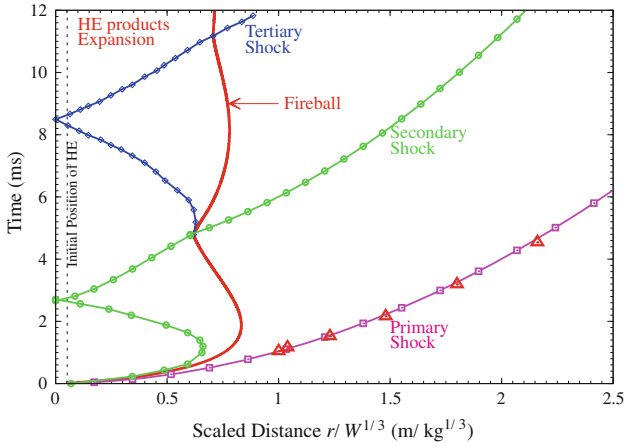

Fig. 11 Space–time diagram for shocks, fireball interface for Blast Wave propagation in air. Experimental results (*red triangle. with dot*)

calculations for the sub-scale experiments are less than 10 %. For the 6.6 kg case, it can be seen that only results for the gauges under 1.5 m/kg$^{1/3}$ are satisfying compared with the Kinney and Graham data. The possible measurement errors as well the different afterburning behavior can explain these discrepancies. Omang et al. [32] also pointed out the difficulty to measure accurately these quantities.

From the scattered experimental results, it is difficult to confirm any scaling law for the BW propagation in the AF, even if the points are close to the Sandia NEST fit. One possible reason could be the different physico-chemical properties of the AF used in the sub as well as in the full-scale experiments. However, this is also in accordance with [20] where the authors also reported marginally successful scaling between experiments of 50 and 1 lb of C4 in AF of ER 1:60.

In air, good agreement between numerical results and KG database is achieved for a scaled distance above 1. In AF, no general scaling law as for the experimental results can be reported. Nevertheless, the numerical results did show scaling for the full-scale charges, as for the peak overpressures.

5.3 Wave diagram for blast wave propagation

From the numerical results, the location of the fireball, the main shock as well as the subsequent ones as function of time are plotted in Fig. 11, in the case of BW propagation in air and in Fig. 12 and in the case of BW propagation in AF.

The space-time diagram in air has been described by Brode [11] and is recalled here. As the acoustic impedance of air is very low compared with that of the detonation products, the shock wave in air starts with an initial strength weaker than that of the CJ high pressure and decays with the spherical divergence. This primary shock is responsible for the maximum peak overpressure. There is a good agreement between

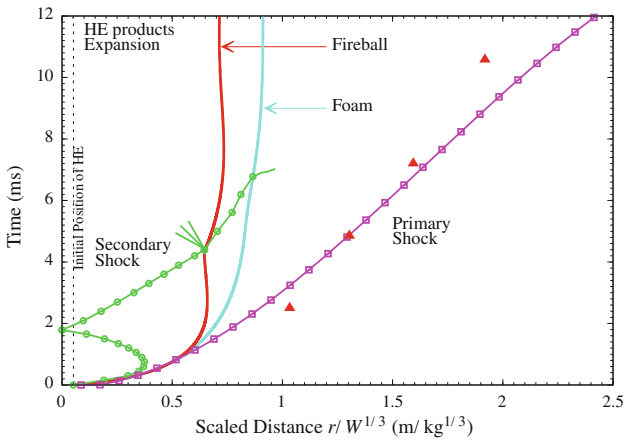

Fig. 12 Space–time diagram for shocks and interfaces for Blast wave propagation in aqueous foam. Experimental results (*filled red triangle*)

the numerical results and the measurements results for the time of arrival of the primary shock (see Fig. 11). A secondary shock then develops, which follows the rarefaction waves. This shock grows as it moves inward, then implodes and reflects on the origin. Meanwhile, the detonation products have ended their expansion and are beginning to shrink. The interaction of the secondary shock with the fireball interface inverts abruptly its trajectory and results, as for the first time, in an outward secondary shock and inward rarefaction waves, followed by a tertiary shock. This process of subsequent shock formation repeats until the energy of the detonation products is dissipated.

The space–time diagram for shocks and the different interfaces in the case of BW propagation in Aqueous Foam is depicted in Fig. 12. There is a fairly good agreement between the numerical and experimental results for the time of arrival of the primary compression waves. The first difference with the case of air is the presence of the permeable AF interface. Indeed, the liquid and the gas of the AF are initially pushed away from the explosion origin, during the expansion of the HE products, but behave differently due to their different inertia. The liquid phase has its own velocity and dynamics. Thus, as the gas phase contracts thereafter, the greater inertia of the liquid phase tends to project the AF far from the fireball. The same qualitative features have been described in [43]. The presence of a new gap, composed of air, which lies between the AF and the fireball, ensues. This results in a more complex pressure wave propagation, due to the creation of the new multiphase interface and to the extra wave pattern. Another difference is that the time of arrival of the primary shock in the case of aqueous foam is twice of that in air. This can be explained by the lowered speed of sound of Wood. Moreover, since the foam has a higher density and a higher acoustic impedance, the velocity of the fireball, which acts as a piston on the environment is lower. In addition, the created gap tempers the amplitude of pressure and total energy of the transmitted shock wave to the aqueous foam, as explained by Seitz and Skews [44]. This results in a lower overpressure field (see Fig. 7) for the spherical decaying shock wave and a final position of the fireball which is at a smaller scaled distance. The oscillating character of the fireball is also less marked in foam. The time at which the secondary shock implodes at the origin is shorter as the initial inward rarefaction waves are weaker. And then, the secondary shock impacts the fireball interface at the same time as the contracting phase begins.

5.4 Overpressure time histories

Figures 13 and 14 show the pressure–time histories for the air and the AF configurations.

In the case of BW in air, the computational results are in good agreement with the experimental data for the primary shock (see Fig. 13). The profile of blast wave is retrieved with a sharp pressure jump, followed by a pressure decrease. Later, there is some deviation, probably due to the afterburning of rest products, enhanced by turbulent mixing, generated by multidimensional Rayleigh–Taylor and Richtmyer–Meshkov instabilities, which are not taken into account by the model.

In the case of BW in AF, a parametric study looked at the effect of droplet size, from 10 to 100 μm. Using a log-log scale, the peak overpressure ratio as a function of the scaled distance was the same. Mainly the two-phase blast wave structure and the time of arrival were affected. In Fig. 14, the numerical results for two radii of 10 and 50 μm are compared with the experimental pressure time histories. A better agreement with experimental data can be seen for the 10 μm case. One can also see the two-phase blast wave structure, as Borisov et al. [6] reported and the role of a relaxing media to enhance mitigation [17,18]. The two-phase BW consists of a two-phase shock wave, followed by a pressure decrease, due to rarefaction waves from spherical divergence. A two-phase shock is a composite shock wave, which consists of a shock wave, followed by a relaxation zone [41]. Here, the liquid phase and the related relaxation zone which undergoes the effects of the rarefaction waves from spherical divergence, act to disperse the energy from the sharp shock peak and to smooth the latter [42]. This explanation holds when we are not close to the charge. Indeed, at the beginning of the interaction of the detonation front with the surrounding media, the time scale of the velocity relaxation will be very short and the phases are almost in equilibrium. Thus, as the acoustic impedance of the foam is greater than air (see Fig. 3), the overpressure of the transmitted shock wave will be higher. The numerical results (see Fig. 8) have shown that this transition occurs at a scaled distance of 0.3.

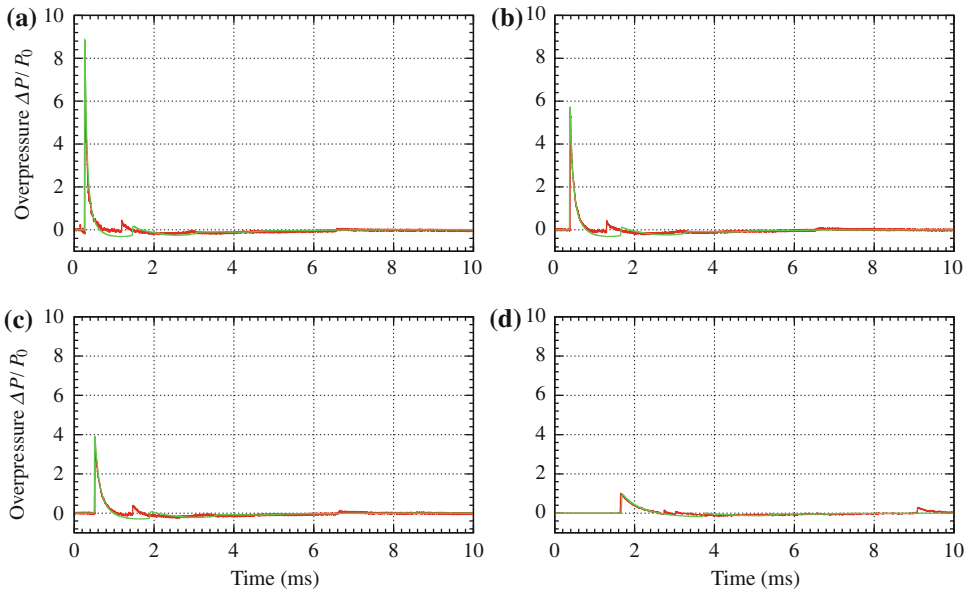

Fig. 13 Comparison between experimental pressure signals in *red lines* and computational results in *green lines* for the detonation of a 145 g HE charge in air for scaled distances of **a** 0.97 m/kg$^{1/3}$, **b** 1.16 m/kg$^{1/3}$, **c** 1.35 m/kg$^{1/3}$ and **d** 2.51 m/kg$^{1/3}$

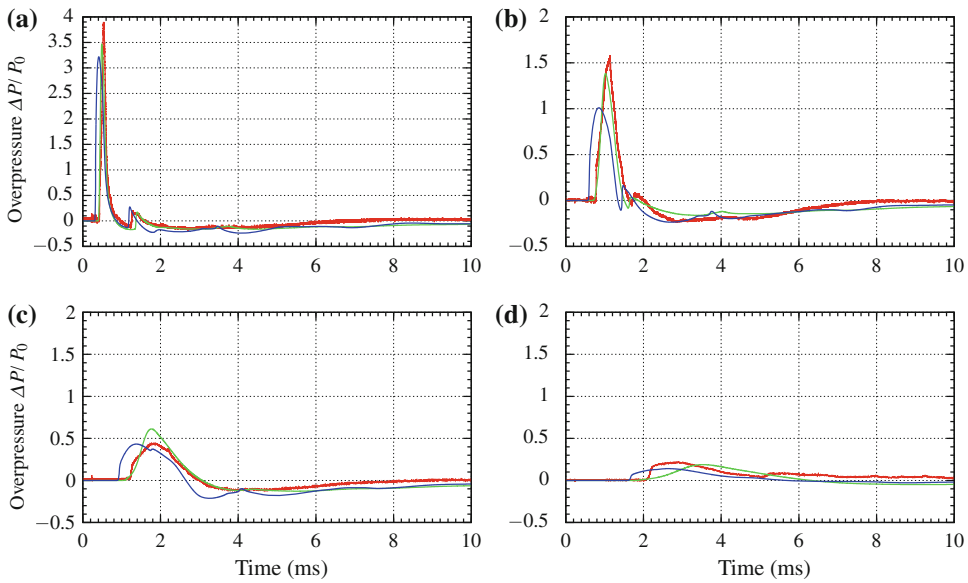

Fig. 14 Comparison between experimental pressure signals in *red lines* and computational results with droplets radii of 10 μm in *green lines* and 50 μm in *blue lines* for the detonation of a 145 g HE charge in a foam of expansion ratio 1:120 for scaled distances of **a** 0.72 m/kg$^{1/3}$, **b** 0.94 m/kg$^{1/3}$, **c** 1.17 m/kg$^{1/3}$ and **d** 1.63 m/kg$^{1/3}$

6 Summary and conclusions

In this paper, a multiphase approach is used to model the dry aqueous foam as a dense non-equilibrium two-phase medium and its interaction with the HE detonation products. After the shock impingement, the initially encapsulated gas pores and liquid ligaments become, respectively, the carrier phase and the dispersed phase composed of liquid droplets. Conventional constitutive relations have been used to describe the inter-phase exchanges between gas and droplets. Additionally, new experiments are performed to study the scaling effects.

Good agreement was found between the numerical and the experimental results, which show the mitigation properties of the BW by aqueous foams. In middle field range of scaled distances greater than one, the peak overpressure reduction can reach 10 up to 20. The reduction in scaled impulse was less marked, gradually increasing above the scaled distance of one.

From the experimental data, one can conclude that the Hopkinson $W^{1/3}$ scaling law still holds for the peak overpressure ratio, whereas it is more difficult to assess this assumption for scaled impulses. The latter is, however, difficult to measure accurately. Nevertheless, the numerical results

show that this scaling holds particularly for overpressures and scaled impulses in the case of full-scale experiments. This means that the non-equilibrium processes have enough time to reach equilibrium. A numerical study indicates that the characteristic size of PB plays a secondary role.

The non-equilibrium processes due to momentum and energy transfers are shown to have two effects. The first one concerns the local structure of the two-phase BW, which has been investigated from pressure time histories. Experimental as well as numerical results show that it consists of a shock wave, followed by a relaxation zone, further followed by a pressure decrease. This results in the energy dispersion at the peak overpressure. The second one concerns the structure of the wave diagram. Its shows the creation of a buffer between the fireball interface and the aqueous foam, which is due to non-equilibrium effects. Moreover, the velocity of the fireball was smaller in the AF configuration. As a consequence, this results in a lower overpressure of the two-phase spherical decaying shock wave.

Acknowledgments A. Chinnayya would like to thank Prof. R. Saurel, IUSTI, Marseille France for fruitful discussion and the French Atomic Energy Commission (CEA) for financial support.

Appendix A: JWL equation of state

The detonation products are described by the JWL (Jones-Wilkins-Lee) equation of state [29]. The use of the formalism of [5] yields the following:

$$e = e_{\rm is} + C_v T$$
$$p = p_{\rm is} + \Gamma_0 \rho (e - e_{\rm is})$$

with $p_{\rm is}$ the isentrope pressure issued from the Chapman–Jouguet (CJ) state.

$$p_{\rm is}(\rho) = p_{k1}(\rho) + k\left(\frac{\rho_0}{\rho}\right)^{-(1+\Gamma_0)}$$

where $p_{k1}(\rho) = A\exp\left(-R_1\frac{\rho_0}{\rho}\right) + B\exp\left(-R_2\frac{\rho_0}{\rho}\right).e_{\rm is}$ and $p_{\rm is}$ are linked by the following relation: $\frac{de_{\rm is}}{d(1/\rho)} = -p_{\rm is}$. Thus

$$e_{\rm is}(\rho) = c_{ek} + \frac{A}{\rho_0 R_1}\exp\left(-R_1\frac{\rho_0}{\rho}\right) + \frac{B}{\rho_0 R_2}\exp\left(-R_2\frac{\rho_0}{\rho}\right) + \frac{k}{\rho_0\Gamma_0}\left(\frac{\rho_0}{\rho}\right)^{-\Gamma_0}$$

The different constants are given by

$$\frac{1}{\rho_{\rm CJ}} = \frac{1}{\rho_0} - \frac{p_{\rm CJ}}{\rho_0^2 D_{\rm CJ}^2} \text{ (Rayleigh line)}$$
$$e_{\rm CJ} = e_0 - \frac{p_{\rm CJ}}{2}\left(\frac{1}{\rho_{\rm CJ}} - \frac{1}{\rho_0}\right) \text{ (Hugoniot equation)}$$

The constants k and c_{ek} are such that $e = e_{\rm CJ}$ and $p = p_{\rm CJ}$ in the EOS

$$c_{ek} = e_{\rm CJ} - e_{\rm is}(\rho_{\rm CJ}) - \frac{p_{\rm CJ} - p_{k1}(\rho_{\rm CJ})}{\rho_{\rm CJ}\Gamma_0}$$
$$k = \left[p_{\rm CJ} - p_{k1}(\rho_{\rm CJ}) - \frac{C v \rho_{\rm CJ} T_{\rm CJ}}{\Gamma_0}\right]\left(\frac{\rho_{\rm CJ}}{\rho_0}\right)^{1+\Gamma_0}$$

The CJ parameters can be determined by a CJ thermochemical code. The JWL equation of state corresponds to a reduction of a more complete EOS as for example the H9 EOS [21]. The different JWL parameters for the present computations are for the TNT energetic material and are taken from literature: $\rho_0 = 1,630$ kg/m^3, $A = 3.712.10^{11}$ Pa, $B = 0.03231.10^{11}$ Pa, $R_1 = 4.15$, $R_2 = 0.95$, $\Gamma_0 = 0.3$ [45], $p_{\rm CJ} = 19$ GPa, $D_{\rm CJ} = 6,950$ m/s, $T_{\rm CJ} = 3669$ K [21], $C_v = 2345$ J/kg K [22], $e_0 = 0$ J/kg.

Appendix B: Equation of state for the liquid and the gaseous phases of the aqueous foam

The liquid of the aqueous foam is modeled by the Stiffened Gas EOS. A method which gives the overall procedure to determine these constants is given in [28]. The Stiffened Gas EOS for the liquid phase can be summarized as

$$P_1 + P_{\infty,1} = \frac{\gamma_1 - 1}{\gamma_1} C_{{\rm p},1}\rho_1 T_1$$
$$e_1 = e_{0,1} + \frac{P_1 + \gamma P_{\infty,1}}{(\gamma_1 - 1)\rho_1} \quad (18)$$

We followed the procedure given in [28] to determine the thermodynamic parameters of the liquid phase. The parameters are calculated from the experimental saturation curves (cf. [14]). From [28], they are calibrated from two reference states. For the liquid phase, the two states are 439 and 588 K. The thermodynamic parameters are approximately the same as those found in [28]. The constants for the liquid phase are

$$\gamma_1 = 1.49, \quad P_{\infty 1} = 1.063.10^9 \text{Pa},$$
$$C_{\rm p1} = 4,277.77 \text{ J/kg K},$$
$$e_{01} = -0.117.10^7 \text{ J/kg}, \quad s_{01} = 0.0 \text{ J/kg K} \quad (19)$$

The gaseous phase is treated as an ideal gas, with the ratio of specific heats 1.4 and the specific heat at constant pressure $C_{\rm p2} = 1$ kJ/kg K. The ideal gas EOS reads

$$P_2 = \rho_2 r T_2, \quad r = \frac{R}{M} = \frac{\gamma_2 - 1}{\gamma_2} C_{\rm p2}$$
$$e_2 = \frac{P_2}{(\gamma_2 - 1)\rho_2} \quad (20)$$

Table 2 Table of gauge positions and results of the experiments in air conducted on CEA pyrotechnical site

Gauges n°	Experiments in air					
	145 g			6.6 kg		
	SD	$\Delta P/P_0$	$I/W^{1/3}$	SD	$\Delta P/P_0$	$I/W^{1/3}$
1	0.97	8.49	0.99	1	9.49	1.05
2	1.16	5.28	0.93	1.04	8.97	0.83
3	1.35	3.46	0.82	1.23	7.17	1.06
4	1.95	1.85	–	1.48	4.49	1.08
5	2.34	1.07	–	1.8	2.50	1.03
6	2.51	0.96	0.61	2.16	1.72	0.99
7	2.74	1.06	–	2.51	1.29	0.85
8	3.3	0.51	0.46			
9	3.41	0.58	0.47			

SD ($m/kg^{1/3}$) is the scaled distance. $\Delta P/P_0$ is the peak overpressure ratio, $P_0 = 1.01325$ bar. $I/W^{1/3}$ (bar $ms/kg^{1/3}$) is the scaled positive impulse related to the HE mass

Table 3 Table of gauge positions and results of the experiments in aqueous foam conducted on CEA pyrotechnical site

Gauges n°	Experiments in aqueous foam								
	145 g			6.6 kg			22.17 kg		
	SD	$\Delta P/P_0$	$I/W^{1/3}$	SD	$\Delta P/P_0$	$I/W^{1/3}$	SD	$\Delta P/P_0$	$I/W^{1/3}$
1	0.72	3.87	0.94	1.03	1.83	0.88	0.72	5.29	0.89
2	0.9	2.50	1.05	1.11	0.87	0.32	0.74	7.09	1.13
3	0.94	1.57	1.13	1.30	0.52	0.79	0.78	2.66	0.64
4	1.17	0.44	0.82	1.59	0.18	0.61	0.86	2.10	0.64
5	1.63	0.21	1.34	1.92	0.13	0.63	1.05	1.02	0.85
6				2.24	0.10	0.52	1.18	0.61	0.79
7				2.56	0.07	0.40	1.34	0.38	0.69
8							1.45	0.24	0.51

where M is the molar mass, R is the perfect gas constant and C_{p2} the calorific capacity at constant pressure.

Appendix C: Experimental results obtained during the CEA pyrotechnical campaigns

Tables 2 and 3 summarize the experimental results obtained during the CEA pyrotechnical campaigns.

References

1. Allen, R.M., Kirkpatrick, D.J., Longbottom, A.W., Milne, A.M., Bourne, N.K.: Experimental and numerical study of free-field blast mitigation. In: M. Furnish, Y. Gupta, J. Forbes (eds.) Shock Compression of Condensed Matter, 20–25 July 2003, Portland, Oregon (USA), AIP Conference Proceedings, vol. 706, pp. 823–826 (2004)
2. Baer, M.: A numerical study of shock wave reflections on low density foam. Shock Waves **2**((2), 121–124 (1992)
3. Baer, M., Nunziato, J.: A two-phase mixture theory for the deflagration-to-detonation transition (DDT) in reactive granular materials. Intern. J. Multiph. Flow **12**((6), 861–889 (1986)
4. Baker, W.: Explosion in Air. University of Texas Press, Austin (1973)
5. Baudin, G., Serradeill, R.: Review of Jones-Wilkins-Lee equation of state. In: Soulard, L. (ed.) European Physical Journal Web of Conferences, New Models and Hydrocodes for Shock Wave Processes in Condensed Matter, 24–28 May 2010, Paris (France), vol. 10, p. 21 (2010)
6. Borisov, A.A., Gelfand, G.E., Kudinov, V.M., Palamarchuk, B.I., Stepanov, V.V., Timofeev, E.I., Khomik, S.V.: Shock waves in water foams. Acta Astronaut. **5**(11–12), 1027–1033 (1978)
7. Britan, A., Liverts, M., Ben-Dor, G.: Shock wave propagation through wet particulate foam. Colloids Surf A Physicochem Eng Aspects **382**(1–3), 145–153 (2011)
8. Britan, A., Zinovik, I., Levin, V.: Breaking up foam with shock waves. Combust. Explos. Shock Waves **28**((5), 550–557 (1992)
9. Britan, A.B., Ben-Dor, G., Shapiro, H., Liverts, M., Shreiber, I.: Drainage effects on shock wave propagating through aqueous foams. Colloids Surf. A Physicochem. Eng. Aspects **309**(1–3), 137–150 (2007)

10. Britan, A.B., Vasil'ev, E.I., Kulikovskii, V.A.: Modeling the process of shock wave attenuation by a foam screen. Combust. Explos. Shock Waves **30**(3), 389–396 (1994)
11. Brode, H.L.: Blast wave from a spherical charge. Phys. Fluids **2**(2), 217–229 (1959)
12. Chinnayya, A., Daniel, E., Saurel, R.: Modelling detonation waves in heterogeneous energetic materials. J. Comput. Phys. **196**(2), 490–538 (2004)
13. Crepeau, J., Needham, C., Caipen, T., Grady, D., Harper, F.: First principles calculations of the interaction of blast waves with aqueous foams. In: Furnish, M., Chhabildas, L., Hixson, R. (eds.) Shock Compression of Condensed Matter, 27 June–2 July 1999, AIP Conference Proceedings, vol. 505, pp. 779–782. Snowbird, Utah (USA) (2000)
14. COOLPACK: A Collection of Simulation Tools for Refrigeration, 2000, Department of Mechanical Engineering, Technical University of Denmark. http://www.et.web.mek.dtu.dk/coolpack/uk/index.html
15. Domergue, L., Nicolas, R., Marle, J.C., Mathey, L., D'aloisio, M., Buche, L., Hubert, C.: Shock wave attenuation in aqueous foam. In: 3rd International Conference on Safety and Security Engineering, Book Series: WIT Transactions on the Built Environment, Safety and Security Engineering III, vol. 108, pp. 83–92. Rome, Italy (2009)
16. Gardiner, B., Dlugogorski, B., Jameson, G., Chhabra, R.: Yield stress measurements of aqueous foams in the dry limit. J. Rheol. **42**(6), 1437–1450 (1998)
17. Gelfand, B.E.: Attenuation of blast waves in two-phase mixtures. In: Proceedings of the International Symposium on Interdisciplinary Shock Wave Research, ISISW, 22–24 March. http://iswi.nuae.nagoya-u.ac.jp/ISISW/ISISW.html, pp. 150–166. Sendai, Japan (2004)
18. Gelfand, B.E., Silnikov, M.V.: Explosions and Blast Control. Asterion, Saint Petersburg (2004)
19. Goldfarb, I., Orenbakh, Z., Shreiber, I., Vafina, F.: Sound and weak shock wave propagation in gas–liquid foams. Shock Waves **7**(2), 77–88 (1997)
20. Hartman, W., Boughton, B., Larsen, M.: Blast mitigation capabilities of aqueous foam. Tech. Rep. SAND2006-0533, Sandia National Laboratories (2006)
21. Heuzé, O.: Equations of state of detonation products: Influence of the repulsive intermolecular potential. Phys. Rev. A **34**(1), 428–432 (1986)
22. Heuzé, O.: An equation of state for detonation products for hydrocode calculations. In: 27th International Pyrotechnics Seminar (IPS-2000), 16–21 July, pp. 15–19. Grand Junction, Colorado (USA) (2000)
23. Johnson, J.A., Solie, D.J., Brown, J.A., Gaffney, E.S.: Shock response of snow. J. Appl. Phys. **73**(10), 4852–4861 (1993)
24. Kinney, G., Graham, K.: Explosives shocks in Air, 2nd edn. Springer, Berlin (1985)
25. Knudsen, J.G., Gauvin, W.H.: Fluid Mechanics and Heat Transfer. pp. 511 McGraw-Hill, New York (1958)
26. Lallemand, M.H., Chinnayya, A., Le Métayer, O.: Pressure relaxation procedures for multiphase compressible flows. Int. J. Num. Methods Fluids **49**(1), 1–56 (2005)
27. Larsen, M.: NEST containment calculator. Tech. Rep. SAND94-2030, Sandia National Laboratories (1994)
28. Le Métayer, O., Massoni, J., Saurel, R.: Elaboration des lois d'état d'un liquide et de sa vapeur pour les modèles d'écoulements diphasiques. Int. J. Thermal Sci. **43**(3), 265–276 (2004)
29. Lee, E.L., Horning, H.C., Kury, J.W.: Adiabatic expansion of high explosives detonation products. Tech. Rep. TID 4500-UCRL 50422, Lawrence Radiation Lab., University of California, Livermore (1968)
30. Massoni, J., Saurel, R., Lefrançois, A., Baudin, G.: Modeling spherical explosions with aluminized energetic materials. Shock Waves **16**(1), 75–92 (2006)
31. Needham, C.E.: Blast Waves. Springer, Berlin (2006)
32. Omang, M., Christensen, S., Børve, S., Trulsen, J.: Height of burst explosions: a comparative study of numerical and experimental results. Shock Waves **19**(2), 135–143 (2009)
33. Ortiz, C., Joseph, D., Beavers, G.: Acceleration of a liquid drop suddenly exposed to a high-speed airstream. Int. J. Multiph. Flow **30**(2), 217–224 (2004)
34. Persson, P.A., Holmberg, R., Lee, J.: Rock blasting and explosives engineering. CRC Press, Boca Raton (1994)
35. Petitpas, F., Saurel, R., Franquet, E., Chinnayya, A.: Modelling detonation waves in condensed energetic materials: Multiphase CJ conditions and multidimensional computations. Shock Waves **19**(5), 377–401 (2009)
36. Plateau, J.A.F.: Statique expérimentale et théorique des liquides soumis aux forces moléculaires. Gaultier-Villards, Paris (1873)
37. PCB: http://www.pcb.com/techsupport/tech_pres.php
38. Raspet, R.: Use of aqueous foam to mitigate demolition noise. Tech. Rep. N-112, United States Army of Corps of Engineers (1981)
39. Raspet, R., Griffiths, S.K.: The reduction of blast noise with aqueous foam. J. Acoust. Soc. Am **74**(6), 1757–1763 (1983)
40. Rouyer, F., Pitois, O., Lorenceau, E., Louvet, N.: Permeability of a bubble assembly: From the very dry to the wet limit. Phys. Fluids **22**(4), 043302 (2010)
41. Rudinger, G.: Some properties of shock relaxation in gas flows carrying small particles. Phys. Fluids **7**(5), 658–663 (1964)
42. Schwer, D., Kailasanath, K.: Blast mitigation by water mist (3) Mitigation of confined and unconfined blasts. Tech. Rep. NRL/MR/6410–03-8658, Naval Research Lab (2003)
43. Schwer, D., Kailasanath, K.: Numerical simulation of the mitigation of unconfined explosion using water-mist. In: Proceedings of the Combustion Institute, vol. 31, pp. 2361–2369 (2007)
44. Seitz, M., Skews, B.: Effect of compressible foam properties on pressure amplification during shock wave impact. Shock Waves **15**(3–4), 177–197 (2006)
45. Sheffield, S., Engelke, R.: Shock Wave Science and Technology Reference Library, vol. 3, chap. Condensed-phase explosives: shock initiation and detonation phenomena, pp. 1–64. Springer, Berlin (2009)
46. Taylor, G.I.: The formation of a blast wave by a very intense explosion. In: Proceedings of the Royal Society London A, vol. 201, pp. 159–174 (1950)
47. Weaire, D., Hutzler, S.: The Physics of Foams. Oxford University Press, Oxford (1999)
48. Winfield, F., Hill, D.: Preliminary results on the physical properties of aqueous foams and their blast attenuating characteristics. Tech. Rep. DRES, Technical Note No. 389, Defense Research Establishment, Suffield, Ralston, Alberta, Canada (1977)